Bioactive Materials 8 (2022) 57–70

Contents lists available at ScienceDirect

Bioactive Materials

journal homepage: www.sciencedirect.com/journal/bioactive-materials

Bio-printing of aligned GelMa-based cell-laden structure for muscle tissue regeneration

Hanjun Hwangbo [a,1], Hyeongjin Lee [a,1], Eun-Ju Jin [b,1], JaeYoon Lee [a], Yunju Jo [b], Dongryeol Ryu [b,c,**], GeunHyung Kim [a,c,*]

[a] Department of Biomechatronics Engineering, College of Biotechnology and Bioengineering, Sungkyunkwan University (SKKU), Suwon, 16419, Republic of Korea
[b] Department of Molecular Cell Biology, Sungkyunkwan University School of Medicine (SKKU-SOM), Suwon, 16419, Republic of Korea
[c] Biomedical Institute for Convergence at SKKU (BICS), Sungkyunkwan University, Suwon, 16419, Republic of Korea

ARTICLE INFO

Keywords:
GelMa bio-ink
in-situ crosslinking
3D bioprinting
Myogenesis

ABSTRACT

Volumetric muscle loss (VML) is associated with a severe loss of muscle tissue that overwhelms the regenerative potential of skeletal muscles. Tissue engineering has shown promise for the treatment of VML injuries, as evidenced by various preclinical trials. The present study describes the fabrication of a cell-laden GelMa muscle construct using an *in situ* crosslinking (ISC) strategy to improve muscle functionality. To obtain optimal biophysical properties of the muscle construct, two UV exposure sources, UV exposure dose, and wall shear stress were evaluated using C2C12 myoblasts. Additionally, the ISC system showed a significantly higher degree of uniaxial alignment and myogenesis compared to the conventional crosslinking strategy (post-crosslinking). To evaluate the *in vivo* regenerative potential, muscle constructs laden with human adipose stem cells were used. The VML defect group implanted with the bio-printed muscle construct showed significant restoration of functionality and muscular volume. The data presented in this study suggest that stem cell-based therapies combined with the modified bioprinting process could potentially be effective against VML injuries.

1. Introduction

Discussions regarding volumetric muscle loss (VML) have dominated certain areas of healthcare research in recent years [1]. In particular, the implantation of autologous muscle tissues has been the gold standard strategy for the treatment of VML defects [2]; however, these implants are often ineffective and can even induce implant failure due to low regeneration efficiency resulting from low controllability of the structural organization of myofibers [3]. Thus, tissue engineering strategies have been proposed as an alternative treatment method for VML defects. To fabricate tissue engineering structures, artificial muscle tissue-specific synthetic or natural biomaterials supplemented with various cell types including myogenic progenitor cells and adipose stem cells have been made using different methods [4]. However, sources of endogenous myogenic progenitor cells in adults are often limited and difficult to access. To overcome this issue, several researchers have investigated the myogenic lineage of hASCs for muscle regenerative potentials.

Recently, cell-laden structures have been investigated as promising exogenous biomaterials for regenerating various tissues [5,6]. In particular, myoblasts are loaded in various natural hydrogels, such as alginate, methacrylated gelatin (GelMa), nanocellulose, fibrin, and collagen, as bio-inks, and these can be processed with micro-molding, mechanical or electromagnetic devices, and bioprinting to form a 3D cell-laden complex construct with or without supporting anchors [7]. Although typical biomanufacturing processes have facilitated myotube formation and maturation, bioprinting can allow multi-scalable precise structures that mimic various biophysical and biochemical properties of native tissues, which can be a prerequisite for successfully regenerating the unique parallel tissue structure observed in muscle tissue. Moreover, the bioprinting process can endow controllable 3D spatial cell-positioning with various biomaterials in 3D structures [8,9].

Peer review under responsibility of KeAi Communications Co., Ltd.
* Corresponding author. Department of Biomechatronics Engineering, College of Biotechnology and Bioengineering, Sungkyunkwan University (SKKU), Suwon, 16419, Republic of Korea.
** Corresponding author. Department of Molecular Cell Biology, Sungkyunkwan University School of Medicine (SKKU-SOM), Suwon, 16419, Republic of Korea.
E-mail addresses: freefall@skku.edu (D. Ryu), gkimbme@skku.edu (G. Kim).
[1] These authors contributed equally to this work.

https://doi.org/10.1016/j.bioactmat.2021.06.031
Received 3 May 2021; Received in revised form 25 June 2021; Accepted 25 June 2021
Available online 6 July 2021

Recently, Ouyang et al. introduced an *in situ* crosslinking process into a 3D bioprinting process, which can induce the formation of cell-laden hydrogel struts without loss of cell viability [10]. This process can realize a one-step printing process that does not require any post-processing procedures to sustain printed cell-laden hydrogel filaments; however, with respect to cell arrangement, the method did not provide any topographical cue, which is an essential requirement to develop effectively uniaxially aligned myofibers in the printed structure.

Previously, we developed various bioprinting processes to fabricate uniaxially aligned functional cell-laden structures using a pre-incubated methacrylated gelatin (GelMa) bio-ink, collagen fibrillation process, cell-laden gold nanowires/collagen bio-ink, and dECM-MA/fibrillated PVA bio-ink [11–14]. Although these methods provide considerable advantages to cell alignment and uniaxially patterned myotube formation, there are several disadvantages such as the difficulty in obtaining stable rheological properties after incubating the cell-laden bio-ink [11], narrow stable processing conditions to obtain high cell viability [12], additional electric field to control the Au nanowires in the bio-ink [13], and loss of cells *via* the PVA leaching process [14,15]. Therefore, we need to develop an easier and more versatile bioprinting method to attain a functional cell-laden structure with a topographical cue to be used in the regeneration of skeletal muscles or aligned tissue structures.

In this study, we attempted to obtain cell-laden structures that consisting of GelMa and C2C12 or GelMA and hASCs cells. The present study elaborates upon the *in situ* crosslinking system (i.e. UV crosslinking at the nozzle) developed by Ouyang et al. to fabricate aligned muscle construct for effective treatment against volumetric muscle loss (VML) [10]. To achieve the uniaxial cellular alignment, we have investigated various parameters including barrel temperature, number of UV light sources, UV exposure dose, and wall shear stresses. Compared to previous systems, the present system offers a simple procedure to achieve the uniaxial cellular alignment by using a modified *in situ* crosslinking process of GelMA. The modified crosslinking process was supported by two UV exposure systems and a glass nozzle attached to the printing barrel. By controlling the UV exposure dose (UV power and crosslinking time) and wall shear stress within a nozzle, we measured the initial cell viability and cell alignment using C2C12 cells. The shear-induced alignment of the cells was analyzed using the morphological structure of F-actin and the myotube heavy chain (MHC). In addition, to observe the regeneration of muscle tissue, the myogenic gene expression of the cell-laden constructs was assessed and compared to the normally printed cell-laden GelMa structure. Additionally, to ensure that the optimized printing parameters for C2C12 cells have a similar effect on hASCs, we have conducted experiments on ISC and CC structures ladened with hASCs. As expected, cellular orientation and MHC expressions were significantly higher on the ISC structure. Finally, the bio-printed structures laden with human adipose-derived stem cells (hASCs) were implanted in a mouse model and assessed as a potential bioartificial muscle construct *in vivo*. Based on the *in vivo* results, we conclude that the *in situ* crosslinked cell-laden GelMa constructs with an aligned cell structure can be a new promising platform for encouraging a high degree of myogenesis.

2. Methods

2.1. Methacrylation process of gelatin

Methacrylation of gelatin was conducted based on a previously outlined protocol [11]. Briefly, gelatin (300 g Bloom; Sigma Aldrich) from porcine skin was dissolved in phosphate-buffered saline (PBS) (10% w/v). Methacrylic anhydride (Sigma Aldrich, USA) was added dropwise under continuous stirring at 50 °C. After 2 h, the methacrylated gelatin (GelMA) was dialyzed in distilled water using dialysis tubing at 40 °C for 7 days to remove the remaining methacrylic anhydride. GelMA was lyophilized for use.

2.2. Preparation and characterization of C2C12 GelMA 5 wt% bio-ink

Lyophilized GelMa was dissolved in PBS at a weight fraction of 5 wt % with Lithium phenyl-2,4,6-trimethylbenzoylphosphinate (LAP) (Sigma Aldrich, USA) was added at a concentration of 0.5% (w/v). Then, the GelMa hydrogel was sterilized via filtering through a 0.22 μm syringe filer (Thermo Fisher Scientific, USA). The solution was mixed with the C2C12 murine skeletal muscle cell line (CRL-1772; ATCC, Manassas, USA) or Adipose-derived stem cells (PT-5006; Lonza, Basel, Switzerland) at a density of 1×10^7/mL.

To evaluate the rheological properties of GelMa 5 wt% bio-ink, a rotational rheometer (Discovery HR2; TA Instruments, Inc., USA) with a cone-and-plate geometry (1° angle, 40 mm diameter, 150 μm gap) was used to measure the storage modulus (G) and complex viscosity (η*). The temperature sweep (4–35 °C) of the pre-crosslinked GelMa (5 wt%) was conducted at a frequency of 1 Hz and 1% strain. Frequency sweep (0.1–10 Hz) was conducted at 4 °C and 20 °C with 1% strain. A time sweep of 5 wt% GelMa was conducted for 100 s at various UV doses. To provide UV dosage of 75, 350, 800, and 2000 (mJ/cm^2), UV light was directed towards the GelMA 5 wt% for 30 s with UV intensity of 2.5, 11.7, 26.7, and 66.7 mW/cm^2 respectively.

2.3. Fabrication of cell-laden GelMa scaffold

A three-axis printing system (DTR3-2210 T-SG; DASA Robot, South Korea) coupled with a dispensing system (AD-3000C; Ugin-tech, South Korea) was used to fabricate the cell-laden structures. The barrel temperature (4 °C), nozzle moving speed (10 mm s^{-1}), and glass capillary (nozzle inner diameter = 500 μm, length = 4 cm) (Hirschmann, Eberstadt, Germany) were fixed. During the extrusion process, the bio-ink was simultaneously exposed to a UV dose [(dose = $I_v \times t$; I_v = UV intensity (164.2 mW/cm^2), t = UV exposure time (5s)] of 821 mJ/cm^2 and wall shear stress [$\tau = (D\Delta P)/4L$; τ = wall shear stress, D = nozzle diameter (500 μm), ΔP = pneumatic pressure (100 Pa), L = nozzle length (2 cm)] of 625 Pa for *in situ* crosslinking. The UV intensity was measured with a UV light meter (LS125; Linshang). A UV spot head (LGA-20562, Limtekeu, Incheon, South Korea) controlled by a UV spot controller (LS-20, Limtekeu, Incheon, South Korea) was used to provide ultraviolet waves (λ = 365 nm) for crosslinking.

To fabricate a 3D structure sized ($2 \times 4 \times 1.5$ mm^3) for *in vivo* implantation, the three-axis printing system was used to stack the struts into the desired dimensions. To prevent the struts from delaminating, the printed 3D structure was exposed to UV light (UV dosage = 50 mJ/cm^2).

2.4. Characterization of the fabricated structure

The fabricated constructs were morphologically characterized using a digital camera connected to an optical microscope (BX FM-32; Olympus, Tokyo, Japan). The circularity ($(4\cdot\pi\cdot A)/P^2$) was measured using the ImageJ software (National Institutes of Health, Bethesda, MD, USA). Additionally, to measure the degradation, the fabricated structures were immersed in phosphate buffered saline (PBS) at 37 °C. The weight change compared to the original weight was measured to assess the rate of degradation.

The mechanical properties (compressive and tensile characteristics) of the structures fabricated using CC and ISC systems were analyzed using the universal tensile machine (Toptech 20000; Chemilab, South Korea). To measure the compressive properties, the samples sized $5 \times 5 \times 1$ mm^3 were compressed in unconfined mode. The compressive speed was set at 0.5 mm s^{-1} and a 30 kgf (294.2 N) load cell was used. To measure the tensile properties, the samples sized 30 mm^3 long were stretched at speed of 0.5 mm s^{-1} using a 30 kgf (294.2 N) load cell.

2.5. In vitro cellular activities

The printed structure laden with C2C12 myoblasts was placed into six-well culture plates and cultured in Dulbecco's modified Eagle's medium (DMEM, high glucose; HyClone™, USA) supplemented with 1% penicillin/streptomycin (PS) (Antimycotic; Thermo Fisher Scientific, USA) and 10% fetal bovine serum (FBS, Gemini Bio-Products, USA) with 5% CO_2 at 37 °C. To induce myogenesis, DMEM high glucose with 2% horse serum (horse serum; Sigma Aldrich St Louis, USA) and 1% penicillin were used. Adipose-derived stem cells (PT-5006; Lonza, Basel, Switzerland) were cultured in low-glucose DMEM supplemented with 1% penicillin and 10% FBS. To induce the myogenesis of the hASCs, the fabricated construct was supplemented myogenic medium consisting of low-glucose DMEM containing 10% FBS, 5% horse serum, 0.1 μM dexamethasone, 50 μM hydrocortisone, 1% penicillin [4]. The medium was changed every 2 d.

The viability of the cells was determined by incubation with 0.15 mM calcein AM and 2 mM ethidium homodimer-1 at 37 °C for 1 h, followed by the visualization of live (green) and dead (red) cells using a Carl Zeiss confocal microscope (LSM 700; Carl Zeiss, Germany). The numbers of live and dead cells were counted using the ImageJ software.

The proliferation of C2C12 myoblasts was analyzed using the MTT proliferation assay (Cell Proliferation Kit I; Boehringer Mannheim, Mannheim, Germany), according to the manufacturer's protocol. Briefly, the scaffolds were immersed in 0.5 mg/mL MTT for 4 h at 37 °C, and the absorbance was measured at 570 nm. To avoid the effects of gel influencing tetrazolium activity and formazan dissolution, constructs without cells have been analyzed as blanks and this absorbance value has been taken away from the value of cell ladened constructs.

The nucleus and filamentous actin (F-actin) of the cells were observed and analyzed with DAPI/phalloidin staining. Briefly, the cells were fixated using 3.7% of paraformaldehyde (252549; SigmaAldrich St Louis, USA) for 1 h and permeabilized with 0.1% Triton X-100 (T8787; Sigma-Aldrich St Louis, USA) for 20 min. Then, the samples were immersed in diamidino-2-phenylinodole (DAPI) (dilution ratio = 1:100 in PBS; Invitrogen, Carlsbad, USA) and Alexa Fluor fluorescein phalloidin (red) (dilution ratio = 1:100 in PBS; Invitrogen) for 90 min. The stained cells were visualized using confocal microscopy and analyzed with Image J software for cell density and orientation factor (90°–φ)/90°, φ = Full width at half maximum (FWHM)).

MHC immunofluorescence staining was performed to evaluate the myogenic differentiation. Briefly, the C2C12 laden structures were washed with PBS, and the cells were fixed in 3.7% paraformaldehyde for 1 h at 37 °C. After fixation, the samples were permeabilized with 2% Triton X-100 and treated with 2% bovine serum albumin (Invitrogen, Carlsbad, CA, USA) for 1 h at 37 °C. The samples were subsequently immersed overnight in anti-MHC antibody (1:200 in PBS; MF 20; Developmental Studies Hybridoma Bank, Iowa, USA) at 4 °C. They were then washed with PBS and incubated with a red-conjugated anti-mouse antibody (1:500 in PBS; Abcam, Cambridge, UK) and DAPI (1:100 in PBS) for visualization. Confocal microscopy was used to visualize and capture the fluorescence images, and the ImageJ software was used for quantitative analysis of MHC positive and fusion index.

2.6. Animal model and surgical procedure

The VML defect was modeled in 10-week-old male C57BL/6 mice (DooYeol Biotech, Inc., Seoul, Korea), and all animal procedures were performed accordingly to the protocol approved by the Institutional Animal Care and Research Advisory Committee at Sungkyunkwan University School of Medicine Laboratory Animal Research Center and complied with the regulations by the institutional Ethics Committee (SKKUIACUC2020-09-52-1). Briefly, the mouse was anesthetized using 3% isoflurane, the skin of the lower left leg was incised, and the muscle was separated from the fascia. To induce VML injury, the extensor digitorum longus (EDL) and extensor hallucis longus (EHL) muscles were removed. Approximately 40% of the tibialis anterior (TA) muscles were excised and weighed. The equation y(g) = 0.0017 × body weight (g) – 0.0716 was used to calculate the TA muscle weight of each animal [16].

Then, the bio-printed constructs sized 2 × 4 × 1.5 mm^3 were carefully placed into the defect site and the incised fascia and skin were sutured together. Four groups were subjected to the procedure at two-week intervals (9 animals in total, n = 3 per group): (i) sham control, (ii) defect only, (iii) CC group (treated with conventionally crosslinked GelMA construct ladened with hASCs), and (iv) ISC group (treated *in situ crosslinked* GelMA ladened with hASCs). For implantation, the bio-printed muscle constructs laden with hASCs at a density of 1 × 10^7 cells/mL were cultured in a growth medium for four days.

2.7. Immunohistochemistry examinations

For histological evaluation, TA muscle samples harvested after two weeks were fixed with 4% paraformaldehyde at room temperature for 24 h. The samples were paraffin-embedded and sectioned into 5 μm thick slices. Deparaffinized sections were stained with hematoxylin and eosin (H&E) and Masson's trichrome (MT) to observe the muscle fibers and fibrotic areas. The muscle sections were also stained with MHC antibodies (1:200 in PBS; MF 20; Developmental Studies Hybridoma Bank, Iowa, USA) for 24 h and washed with PBS and incubated with Alexa Fluor 594 secondary antibodies (Invitrogen). Then, the sections were stained again with DAPI (1:500; Abcam) for 10 min. The stained sections were visualized using confocal microscopy.

2.8. Real-time polymerase chain reaction (RT-PCR)

To quantify the myogenic gene expressions of hASCs, markers Myog, Myh4, Myh5 myogenic markers were analyzed *via* RT-PCR after 14 d of culture. Briefly, the total RNA of the hASCs from CC- and ISC- construct were isolated using a Tri reagent (Millipore Sigma). To measure the concentration and purity of the isolated RNA, a spectrophotometer (FLX800T; Biotek, USA) was used. Then, complementary DNA (cDNA) was synthesized from the RNase-free DNase-treated total RNA using a ReverTra Ace qPCR RT Master Mix (Toyobo Co., Ltd., Japan). The synthesized cDNA was used to conduct quantitative RT-PCR. StepOnePlus real-time PCR system (Applied Biosystems, USA) was used to conduct RT-PCR and the expression of the myogenic gene was normalized using expression levels of beta actin (*Actb*). In addition, gene levels of hASCs on CC- structure were set as one-fold. The gene-specific primers used are as follows: human Myog (NM_002479.6; left: 5′ - gct cag ctc cct caa cca −3′, right: 5′ - gct gtg aga gct gca ttc g − 3′), human Actb (NM_001101.5; left: 5′ - tcc aaa tat gag atg cgt tgt t − 3′, right: 5′ - tgc tat cac ctc ccc tgt gt − 3′), human Myh4 (NM_017533.2; left: 5′ - tgc tgg ctt tga gat ctt tg − 3′, right: 5′ - tgc agt ttc tcg ttg gtg aa − 3′), and human Myf5 (NM_005593.3; left: 5′ - cta tag cct gcc ggg aca −3′, right: 5′ - tgg acc aga cag gac tgt tac at − 3′).

2.9. Muscle strength analysis

Grip strength analysis was performed as previously described [17]. Briefly, the hind limb grip strength of each mouse was assessed on a pull-grid assembly attached to a grip strength meter (BIO-G53, BIOSEB, FL, USA) at two weeks after implantation. To obtain maximal strength, each mouse was pulled along a straight line aligned to the grid. The five-time measurement was repeated three times with 5 min intervals between measurements.

2.10. RNA-sequencing and Gene Set Enrichment Analysis (GSEA)

RNA-sequencing including RNA isolation, library preparation, and FASTQ file generation was done by the DNA link (Seoul, Korea). Total RNAs were isolated from the entire TA muscles. The purity of each RNA sample was determined with a NanoDrop8000™ spectrophotometer

(Thermo Scientific™, MA, USA), and the quality of isolated total RNAs was examined with RNA Integrity Number (RIN) value generated by an Agilent Technologies 2100 Bioanalyzer (Agilent Technologies, CA, USA). Total RNA sequencing libraries were prepared according to the manufacturer's instructions (Illumina Truseq Stranded Total RNA Sample Prep kit with Ribo-Zero Plus rRNA Depletion kit (Illumina, CA, USA). One hundred nanograms of total RNAs from each sample was treated for enzymatic ribodepletion with the Illumina Ribo-Zero Plus rRNA Depletion Kit. RNAs were hybridized with DNA probes complementary to rRNAs. Those probes target RNase H to digest rRNA species. The DNA probes were then digested with DNase I, accompanied by a bead purification of the remaining intact RNAs. Following purification, the rRNA-depleted total RNA was fragmented into small pieces using divalent cations. The cleaved RNA fragments were copied into the first strand, cDNA using reverse transcriptase and random primers. This was followed by second-strand cDNA synthesis using DNA Polymerase I and RNase H. These cDNA fragments then had the addition of a single 'A' base and subsequent ligation of the adapter. The products were purified and enriched with PCR to create the final cDNA library. The quality of the amplified libraries was verified by the Tapestation system, an automated electrophoresis (Agilent Technologies, CA, USA). After QPCR using KAPA SYBR FAST qPCR Master Mix (Kapa Biosystems, MA, USA), we combined libraries that index tagged in equimolar amounts in the pool. RNA sequencing is performed using an Illumina NovaSeq 6000 system (Illumina, CA, USA) following provided protocols for 2x100 sequencing. The quality of the raw sequencing data was checked using FastQC (v0.11.9). Sequenced reads were aligned to the mouse reference genome (GRCm39/mm10). Quantification of aligned reads was committed using RSEM v1.2.28 [18]. TPM (Transcripts per Million) was used for further analysis. GSEA was performed as described previously [19]. The visualization of gene expression (heatmap), Spearman's correlation, and gene network were assessed with R packages ggpubr, ggplot2, igraph, ggraph, egg, corrr, corrplot, dplyr, tidyverse, and reshape.

2.11. Statistical analysis

Data are expressed as the mean ± standard deviation (SD). Normally distributed continuous variables were compared using one-way analysis of variance (ANOVA), followed by Tukey's post-hoc test for pairwise comparisons. The student's t-test was performed for comparisons between the two groups. In addition, to test the equality of variance and normality of the data, Levene's test and Shapiro-Wilk test have been performed. If the assumptions are not met, non-parametric equivalent tests (Mann-Whitney test for *t*-test and Kruskal Wallis test for one-way ANOVA) were performed. All statistical analyses were performed using SPSS for Windows (version 18.0; SPSS, Chicago, IL, USA), with $p < 0.05$, defined as statistically significant.

3. Results and discussion

3.1. Development of in-situ UV crosslinking systems

Autologous tissue implantation is a promising strategy for treating VML. To fabricate autologous tissue, 3D bioprinting has been widely used for multilevel customizable geometries. Herein, we utilized a bio-ink (5 wt% GelMa mixed with C2C12 myoblasts at a density of 1×10^7 cells/mL) (Fig. 1A) for an *in situ* crosslinking process, which was supported by two UV light sources (Fig. 1B and C). As a result of the *in situ* crosslinking of the cell-laden GelMa bio-ink, an equidimensional strut was obtained using the homogeneous crosslinking degree of GelMa, indicating that low extrudate swelling ($D_1/D_o = 1.04$) was achieved, as shown in the optical image in Fig. 1C. This indicated that the aligned morphological structure of the printed strut within a nozzle can be well maintained after the extrusion process, as shown in the surface SEM image in Fig. 1C. The schematic in Fig. 1D shows the theoretical alignment mechanism of the GelMa molecular chains processed in the extruding nozzle combined with an *in situ* crosslinking process.

To analyze the viscoelastic properties of the bio-ink (GelMa, 5 wt%), the storage modulus (G') and complex viscosity (η*) were measured *via* rheological testing (Fig. 2). In general, the modulus of the GelMa bio-ink was relatively high at low temperatures (below 10 °C) but viscous at high temperatures (above 20 °C), which indicates a gel–sol transition temperature in the range of 20 °C–30 °C (Fig. 2B). The increase in temperature causes a structural breakdown in GelMa, causing the aforementioned gel–sol transition [20]. The elastic properties can directly affect the shear-induced alignment of hydrogels; therefore, we selected two typical temperatures (4 °C representing the elastic region and 20 °C showing the viscose region) to determine the effect of processing temperature on the GelMa alignment (Fig. 2B). After using the same volume flow rate and the two-UV exposure system with the condition (821 mJ/cm^2), we assessed the cell alignment in the GelMa struts for the two processing temperatures with live (green)/dead (red) and

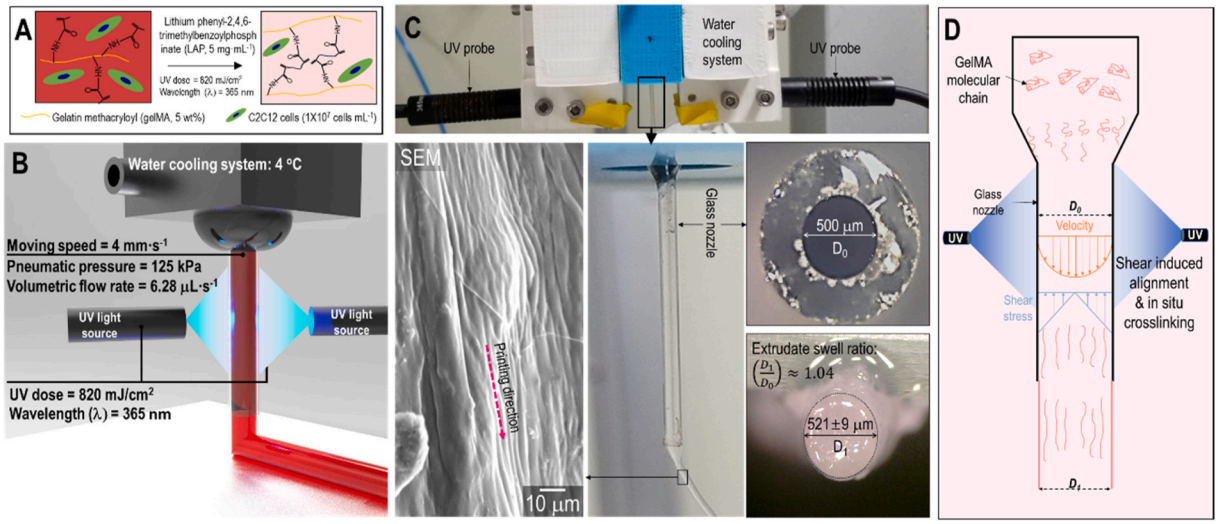

Fig. 1. Schematic of (**A**) GelMa bio-ink and crosslinking process. (**B**) Schematic of *in-situ* crosslinking process using two UV light sources in a bioprinter. (**C**) Optical images of the crosslinking system and a printed GelMa strut indicating alignment and low extrudate swelling. (**D**) Schematic of shear-induced alignment through the nozzle-based extrusion system and in-situ UV crosslinking process (D_o = diameter of the nozzle, D_1 = diameter of extruded strut).

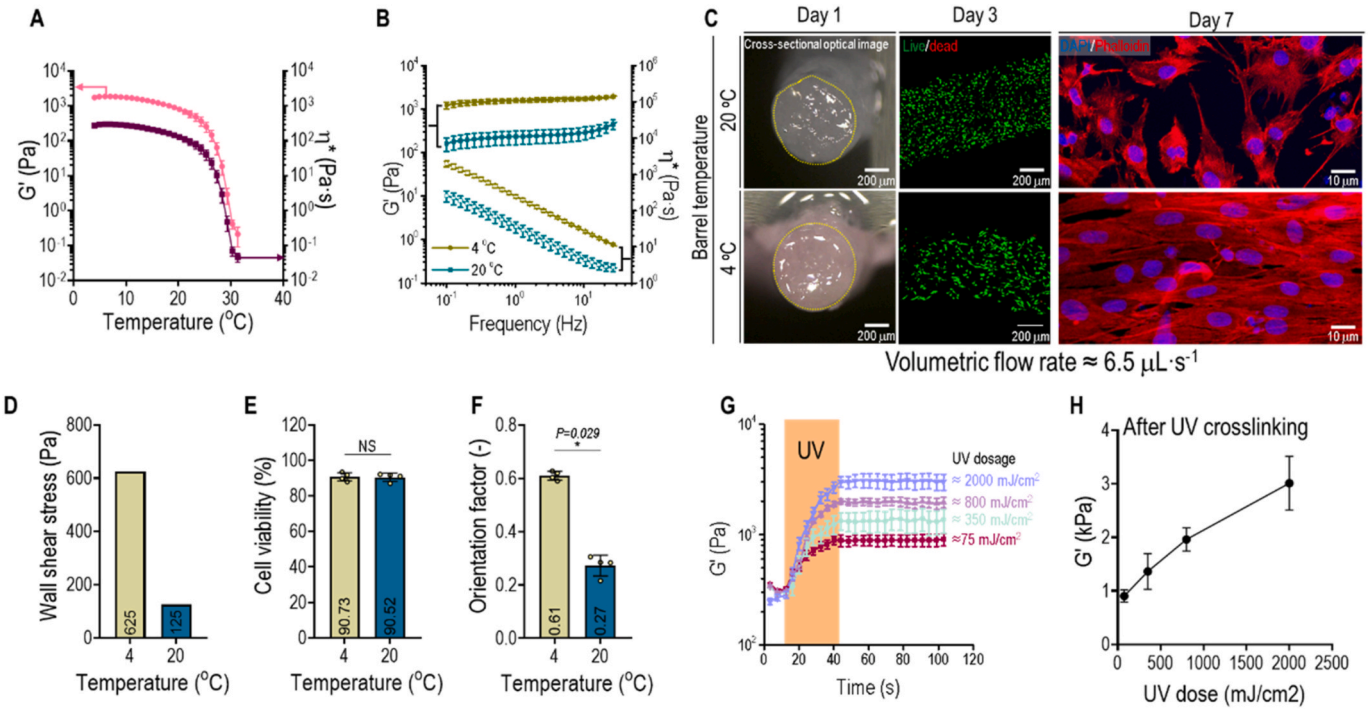

Fig. 2. Rheological properties (G' = storage modulus, η* = complex viscosity) of 5 wt% GelMa of (**A**) temperature sweep, (**B**) frequency sweep. (**C**) optical, live (green)/dead (red) at 1 day, and DAPI (blue)/phalloidin (red) images at 7 days for the cell-laden GelMa struts processed at two different processing temperatures (4 °C and 20 °C). (D) Wall shear stress required to achieve a similar volumetric flow rate for two processing temperatures. Quantitative analysis of (**E**) cell viability at day 3 and (**F**) nucleus orientational factor at day 7. (**G**) Storage modulus of 5% GelMa exposed to different UV doses (75–2000 mJ/cm^2) and (**H**) specific storage modulus after crosslinking with various UV doses (*p < 0.05, **p < 0.005, and ***p < 0.001). (For interpretation of the references to color in this figure legend, the reader is referred to the Web version of this article.)

DAPI (blue)/phalloidin (red) images (Fig. 2C). Owing to the elastic properties of GelMA at 4 °C, the wall shear stress ($\tau = (D\Delta P)/4L$; τ = wall shear stress, τ = wall shear stress, D = nozzle diameter, ΔP = pressure differential, L = nozzle length) required to achieve a similar volume flow rate was 5-fold higher compared to GelMA at 20 °C (Fig. 2D). In addition, both structures showed high cell viability (>90%), but the GelMa structure processed at 4 °C showed a more aligned cytoskeleton at seven days compared to that of the structure at 20 °C due to the much higher wall shear stress occurring at a processing temperature of 4 °C (Fig. 2E and F). Based on these results, we chose to set the barrel temperature at 4 °C to maximize the shear-induced alignment of the GelMa bio-ink. However, the duration of the bioink stored at 4 °C could affect cell viability. To assess this, we have stained the C2C12 myoblasts inside the barrel with live (green)/dead (red) at 0–3 h (Supplementary Fig. 1A). As result, the cell viability of C2C12 myoblasts inside the barrel was relatively high (~90%) up to 1 h and rapidly decreased from 2h. Therefore, we set the maximum printing duration at 1 h (Supplementary Fig. 1B).

In addition, to assess the rheological properties of the GelMa bio-ink for UV exposure, various UV dosages (dosage = 75–2106 mJ/cm^2, exposure time = 30 s) were used (Fig. 2G). As expected, the covalent bonds formed from UV radiation significantly increased the modulus of GelMa. Additionally, a linear increase in modulus with UV dosage was observed with GelMa (Fig. 2H).

3.2. *In-situ crosslinking process using a multi-UV exposure system*

To evaluate the effects of multiple UV exposures during *in situ* crosslinking, config-1 (single UV source), config-2 (two UV sources), and config-3 (three UV sources) with the UV source distributed equidistantly were examined (Fig. 3A). We hypothesize that a multi-UV exposure would provide uniform crosslinking in the printing structure compared to a single UV exposure system, thereby inducing homogeneous stiffness throughout the printed strut and even affecting the degree of biodegradability.

To observe the effect of a variety of UV exposure configurations, cross-sectional optical images of printed struts were obtained at 1, 14, and 28 days (Fig. 3B). The structure showed near-perfect circularity for the config-2 and -3 until 14 days, with circularity, which was measured using "$4\pi(A/P^2)$, where A is area, and P is perimeter" of ≈0.96 after extrusion (Fig. 3C), whereas the circularity of the printed strut fabricated using config-1 was significantly low (≈0.9). In addition, a longer culture period (28 days) induced a significant decrease in circularity, with circularity values of 0.86, 0.89, and 0.90 for config- 1, 2, and 3, respectively. Similarly, as shown in Fig. 3D, config-1 showed a relatively higher degradation compared to config-2 and config-3. This phenomenon is likely due to the difference between homogeneous crosslinking (config-2, config-3) and inhomogeneous crosslinking (config-1), determined by the number of UV exposure sources.

To assess the biological effects of various UV configurations, the extruded structure was stained with live (green)/dead (red), DAPI (blue)/phalloidin (red), and DAPI (blue)/MHC (green) at culture durations of 3, 7, and 14 days, respectively (Fig. 3E). The images were quantitatively analyzed for cell viability at 3 days (Fig. 3F), cell density at 7 days (Fig. 3G), orientation factor of F-actin [(90-φ)/90, φ = full width at half maximum (FWHM)] (Fig. 3H), and positive index (percentage of MHC-positive cells) (Fig. 3I). The results show that all the configurations showed high cell viability (>90%), indicating that the UV dosage (800 mJ/cm^2) can be safe. In addition, config-2 and config-3 showed significantly higher cell densities compared to config-1, owing to their different degradation abilities. Concerning the aligned morphological structure of F-actin and MHC, config-2 and -3 exhibited 1.9-fold and 2.2-fold higher orientation factor, and 2.7-fold and 3.5-fold higher MHC-positive index compared to those of config-1, respectively. Several studies have demonstrated that various cellular activities, including the myogenesis of C2C12 myoblasts, can be reliant on the

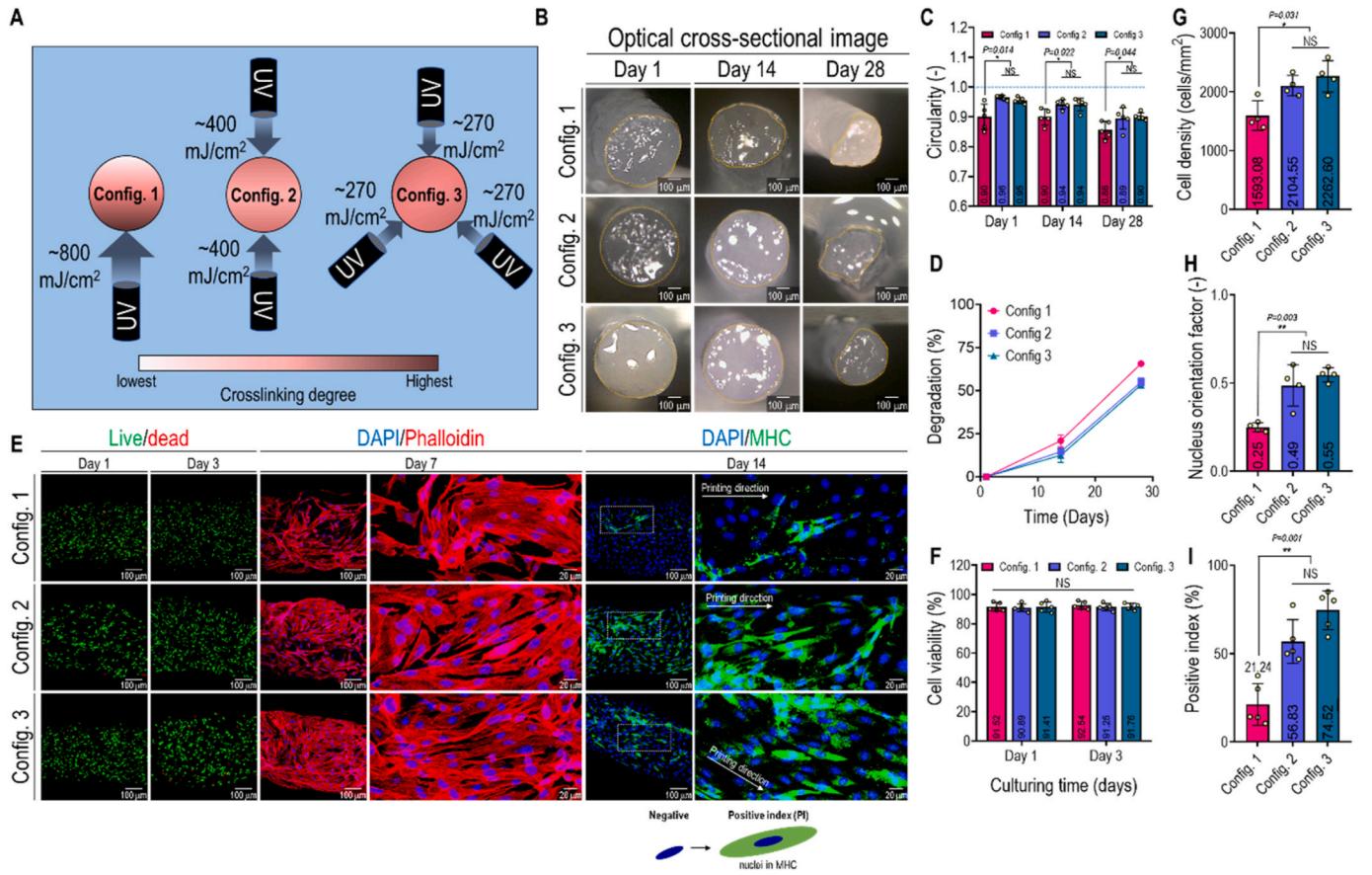

Fig. 3. (**A**) Schematics describing various UV exposure configurations and crosslinking capacity of each of the crosslinking configurations. (**B**) Optical microscopy of cross-sections of the structures extruded with different configurations at 1, 14, and 28 days of culture. (**C**) circularity values and (**D**) degradation graphs measured from optical images. (**E**) Live (green)/dead (red), DAPI (blue)/phalloidin (red), and DAPI (blue)/MHC (green) images at day 3, 7, and 14, respectively. Measured (**F**) cell viability, (**G**) cell density, (**H**) orientation factor, (**I**) positive index of different configurations (*p < 0.05, **p < 0.005, and ***p < 0.001). (For interpretation of the references to color in this figure legend, the reader is referred to the Web version of this article.)

mechanical stiffness of the cell-culturing or cell-encapsulating matrix [21,22]. Therefore, we can estimate that the homogeneous mechanical stiffness of the circular direction of the cell-laden struts, fabricated using two- or three-UV exposure systems can provide more homogeneous and favorable microcellular environmental conditions to induce meaningful development of the cytoskeleton and even myotube formation. Considering the statistical insignificance of cellular density, orientation, and MHC positive index, between config-2 and -3, the dual UV light source (config-2) was sufficient to provide the homogeneous mechanical stiffness of the cell-laden struts. Therefore, we have selected the config-2 crosslinking system for further evaluation as more than two UV light source is unnecessary to achieve similar results.

3.3. Selection of a proper UV-treatment using a config-2 crosslinking device

Regarding the implementation of tissue grafts, suitable degradation of the cell-laden hydrogel is essential for successful tissue regeneration. Additionally, the stiffness of the hydrogel matrix is an important factor to consider when achieving appropriate biological factors [21,22]. In general, elevated UV exposure conditions, such as intensity (I_v) and exposure duration (t), can compromise the integrity of DNA leading to DNA lesions and mutations [23–25]. Although cells have natural inbuilt mechanisms to avoid mutagenesis, however, failure of these mechanisms could induce tumorigenesis [26,27]. Nevertheless, insufficient UV exposure results in rapid structural degradation even before myotube formation.

For these reasons, the proper selection of UV exposure conditions is critical in fabricating mechanically stable and biologically active cell-laden structures. To minimize DNA damage, we have selected a long-wavelength UV light source (λ = 365 nm) to select the optimal UV conditions for *in situ* crosslinking [25]. In addition, combined the two parameters into the UV dose (dose = $I_v \times t$). Various UV doses (75–2106 mJ/cm^2) were used, and Fig. 4A shows cross-sectional optical images at 1, 14, and 28 days. As expected, a higher crosslinking capacity with increased UV dose resulted in the mechanical sustainability of the structure during the culturing period, which was assessed by the circularity values and degradation ability throughout the culture period (Fig. 4B and C).

To qualitatively assess the effects of the UV exposure conditions on the morphological structure and myotube formation of the cultured cells, fluorescence images of the live/dead, DAPI/phalloidin, and DAPI/MHC were used (Fig. 4D). The cells in the structures using UV doses of approximately 821 mJ/cm^2 were safe (above 90% cell viability), but when the dose was increased to 2106 mJ/cm^2, a considerable number of dead cells were observed, presumably due to the harsh UV exposure. However, previous documents have indicated the genotoxic effects with a long-wavelength UV source (λ < 340 nm) [28]. Therefore, although high cell viability was observed with UV dosage up to 821 mJ/cm^2, further investigations are required to assess the genotoxic effects and tumorigenesis.

In addition, as the culture period increased, the cytoskeleton and MHC were well developed, but too high UV exposure conditions can cause lower development of F-actin and MHC formation due to the

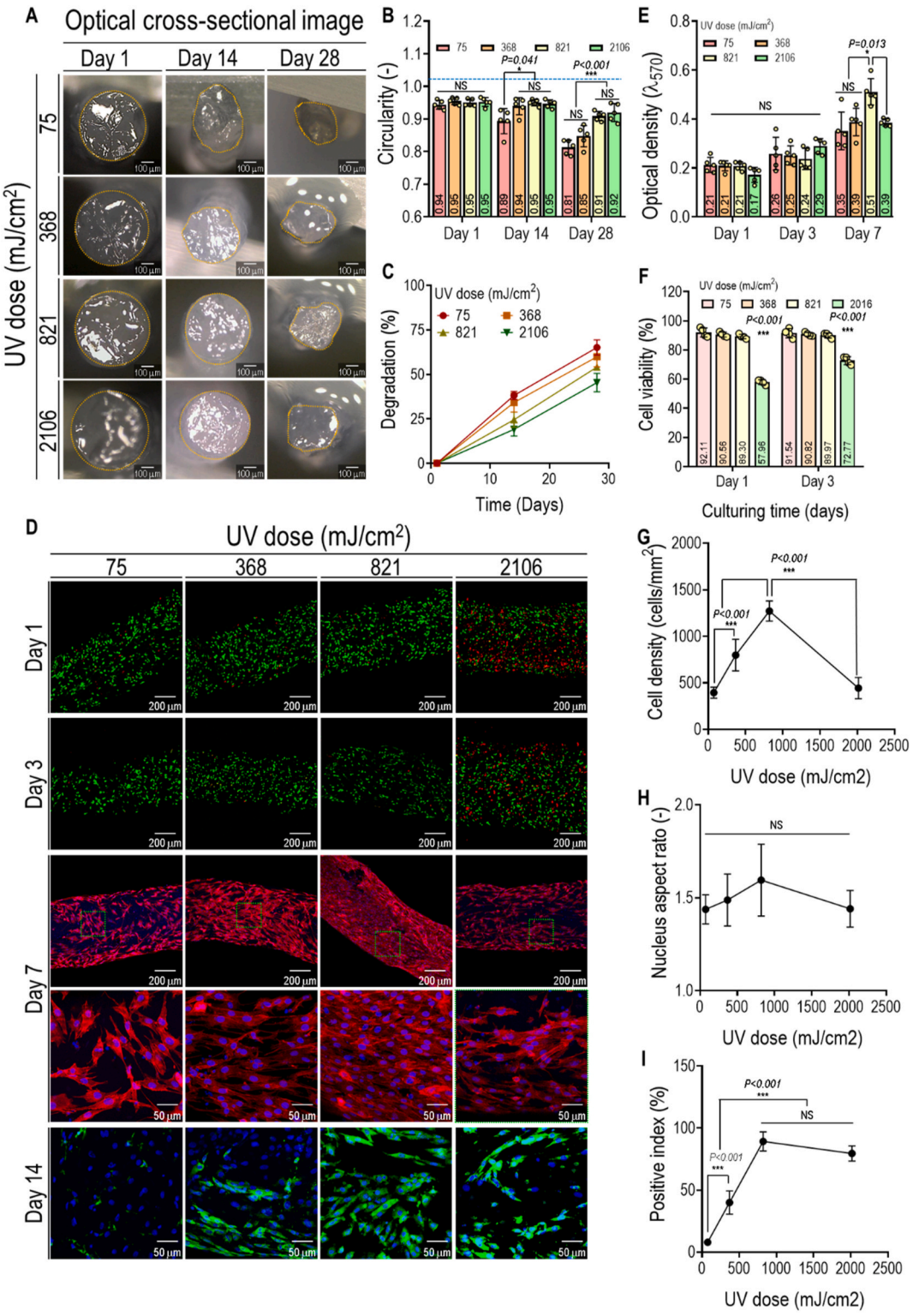

Fig. 4. (**A**) Optical cross-sectional images, (**B**) circularity values, and (**C**) percentage degradation of structures fabricated under different UV doses (75, 368, 821, 2106 mJ/cm^2) with a fixed UV exposure (config-2). (**D**) Immuno/fluorescent images of live (green)/dead (red), DAPI (blue)/phalloidin (red), and DAPI (blue)/MHC (green) images at day 3, 7, and 14, respectively. (**E**) MTT assays of C2C12 proliferation at 1, 3, and 7 days. Measured (**F**) cell viability at day 1, (**G**) cell density and (**H**) aspect ratio at day 7, and (**I**) positive MHC index at day 14. (n = 6, *p < 0.05, **p < 0.005, and ***p < 0.001). (For interpretation of the references to color in this figure legend, the reader is referred to the Web version of this article.)

relatively high stiffness of GelMa, inducing a low degree of cell-cell interaction. For the UV dose of 821 mJ/cm^2, the cytoskeleton and MHC formation were significantly higher compared to others because the appropriate UV conditions can induce a well-adjusted biodegradation rate and mechanical stiffness of the fabricated structure.

The results were validated by quantitative analysis. As indicated by the MTT assays, C2C12 myoblasts proliferated during the culturing period but were significantly higher at a UV dose of 821 mJ/cm^2

(Fig. 4E). This can be attributed to the optimal crosslinking capacity, which provides a suitable platform for cells to proliferate before matrix degradation occurs. However, the UV dose of 2106 mJ/cm^2 resulted in significantly lower cell proliferation due to cell damage, as indicated by cell viability at 1 d (Fig. 4F), and high stiffness caused by the UV dose. Similarly, cell density measured from the density of DAPI (nuclei) staining at day 7 of culture showed a trend similar to that of the cell proliferation (Fig. 4G). The aspect ratio (longest length/shortest length) of the nuclei for the structures exposed to UV doses (75, 368, 821, and 2106 mJ/cm^2) was measured to be 1.44, 1.5, 1.6, and 1.44, respectively (Fig. 4H). Although the aspect ratio was the highest at 821 mJ/cm^2, the values were statistically non-significant, and the positive index shown in Fig. 4I signified a considerably higher myogenic differentiation with increased UV dose, showing 5.0-fold, 11.2-fold, and 10.0-fold higher values for 368, 821, and 2106 mJ/cm^2, respectively, compared to 75 mJ/cm^2. This is because the sufficiently crosslinked GelMa structure can cause more stable MHC formation, whereas insufficiently crosslinked structures can show relatively low mechanical stiffness to fix the shear-induced alignment of the cells [21,22]. Given these results, a UV dose of 821 mJ/cm^2 was selected for further evaluation.

3.4. Shear-induced alignment of the myoblasts

Appropriate microarchitecture is critical for the successful regeneration of muscle tissue because a uniaxially aligned topographical cue of a scaffold could result in successful myogenic differentiation and maturation [29,30]. To attain an appropriate microarchitecture, shear-induced alignment has been regularly investigated owing to its simplicity and cost-effectiveness [31,32]. In this study, we modulated the pneumatic pressure to control the wall shear stress ($\tau = (D\Delta P)/4\,L$); τ = wall shear stress, D = nozzle diameter, ΔP = pressure differential, L = nozzle length, and a wall shear stress of 156–625 Pa was applied to attain appropriate myoblast alignment. To quantitatively analyze the effects of increased wall shear stress, fluorescent images of live/dead cells on day 3, DAPI/phalloidin on day 7, and immunofluorescent images of DAPI/MHC on day 14 were evaluated (Fig. 5A). The cell viability was relatively high (~90%), indicating that the increased wall shear stress was within safe limits (Fig. 5B). To assess the degree of cellular alignment, the distribution of nuclei orientation at 7 days was expressed in the Gaussian form to measure FWHM (φ) (Fig. 5C) and orientation factor, calculated using (90°− φ)/90° (Fig. 5D). Overall, the increase in wall shear stress resulted in a higher degree of alignment of nuclei, indicating that the FWHM was measured to be approximately 68.9°, 64.9°, 43.7°, and 36.7°, and the orientation factor was measured to be 0.23, 0.25, 0.51, and 0.59, with wall shear stresses of 156, 312, 469, and 625 Pa, respectively. We believe that this phenomenon can be attributed to the alignment of the GelMa fibers and cells inside the nozzle *via* shear-induced alignment [33]. Additionally, there was a gradual increase in the nucleus aspect ratio and cell density with the enhanced wall shear stresses due to the more mechanically stimulated cells that can induce an efficient cell-to-cell signaling pathway (Fig. 5E and F) [34]. Since the modulation of the microenvironment could enhance the myogenic differentiation of C2C12 myoblasts [35–38], immunofluorescent images were analyzed: (i) positive index (percentage of cells with MHC coverage), and (ii) fusion index (percentage of MHC-positive cells with two or more nuclei) (Fig. 5G and H). Accordingly, the MHC-positive and fusion indices were gradually enhanced with the increase in shear stress.

By analyzing the data, we noted that the cellular orientation and myogenic differentiating factors (MHC positive index) appears to be stabilizing at wall shear stress of 625 Pa. Similarly, we have previously documented in a logarithmic growth of cellular alignment with wall shear stress owing to the non-spherical and F-actin structures adapting to the flow inside the nozzle [11]. As previous documents have

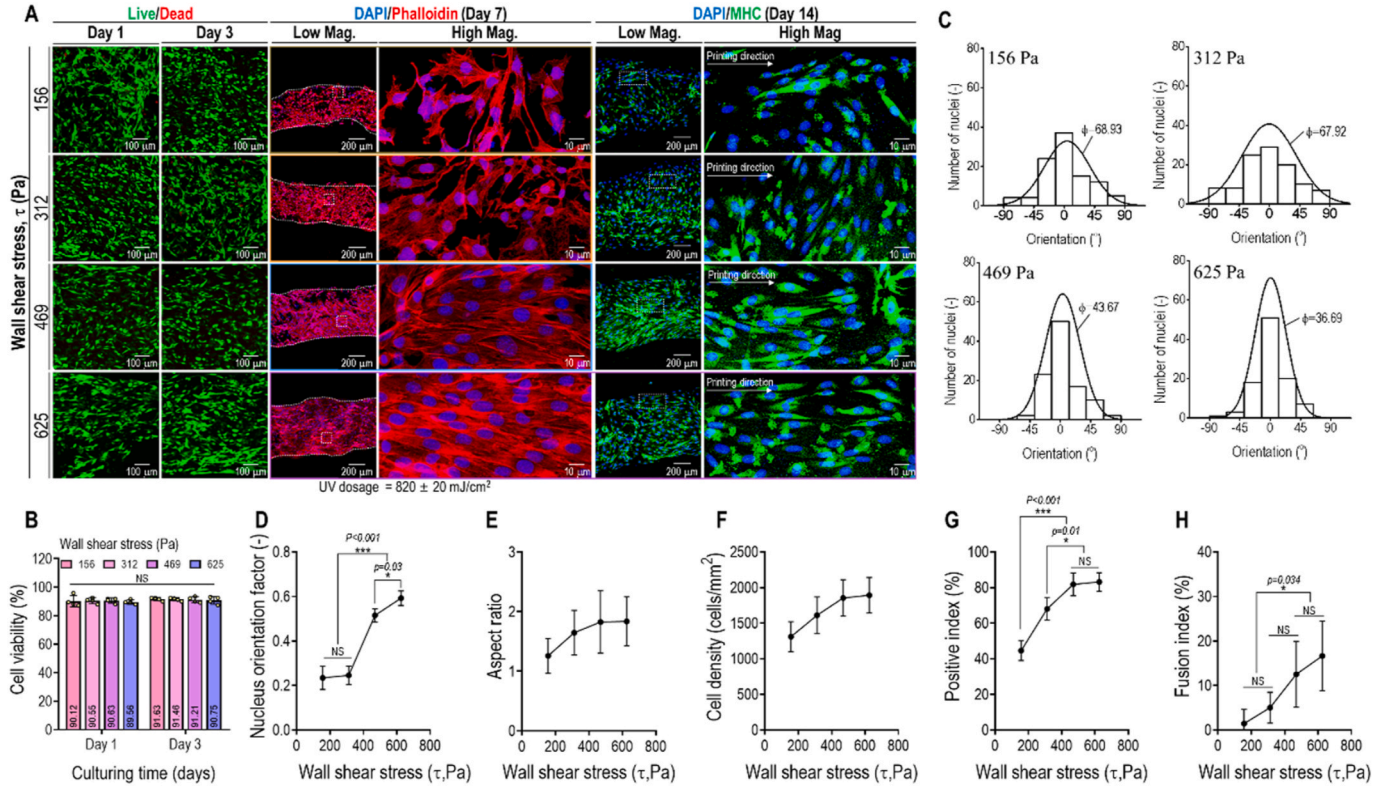

Fig. 5. (**A**) Fluorescence images of live (green)/dead (red), DAPI (blue)/phalloidin (red) and DAPI (blue)/MHC (green) of various wall shear stresses (156, 312, 625 Pa). (**B**) Measured cell viability at day 3. (**C**) Orientation distribution measured from the nuclei orientations at day 7. The effects of increased wall shear stress on (**D**) orientation factor, (**E**) aspect ratio, (**F**) cell density, and MHC (**G**) positive index and (**H**) fusion index. (n = 6, *p < 0.05, **p < 0.005, and ***p < 0.001). (For interpretation of the references to color in this figure legend, the reader is referred to the Web version of this article.)

documented that the increased stress applied to cells can result in loss of cell membrane integrity leading to a loss in cell viability, we have fixed the printing parameters (UV dose of 821 mJ/cm^2 and 625 Pa of wall shear stress) of the C2C12-laden GelMa bio-ink with the crosslinking config-2 device to obtain appropriate biophysical and microcellular environments of the cells [39].

3.5. Comparison of cellular activities of the cell-laden structures fabricated using the normal and modified crosslinking systems

To observe the effects of the modified bioprinting process using *in situ* crosslinking (ISC) on the physical and muscle-specific biological properties of the cell-laden structure, we used a bio-printed structure fabricated using a conventional UV crosslinking (post-crosslinking) system (CC), as shown in Fig. 6A. Fig. 6B shows the cross-sectional and surface optical images and surface SEM images of the printed structures using the CC and ISC crosslinking methods. Accordingly, SEM images indicate an elevated degree of surface alignment with the structures fabricated with the ISC system compared to the CC system. Fig. 6C shows that the circularity of the structure using ISC determined using the cross-sectional image was approximately 0.95 compared to that (~0.8) of the structure using CC, indicating that the crosslinking of the structure (ISC)

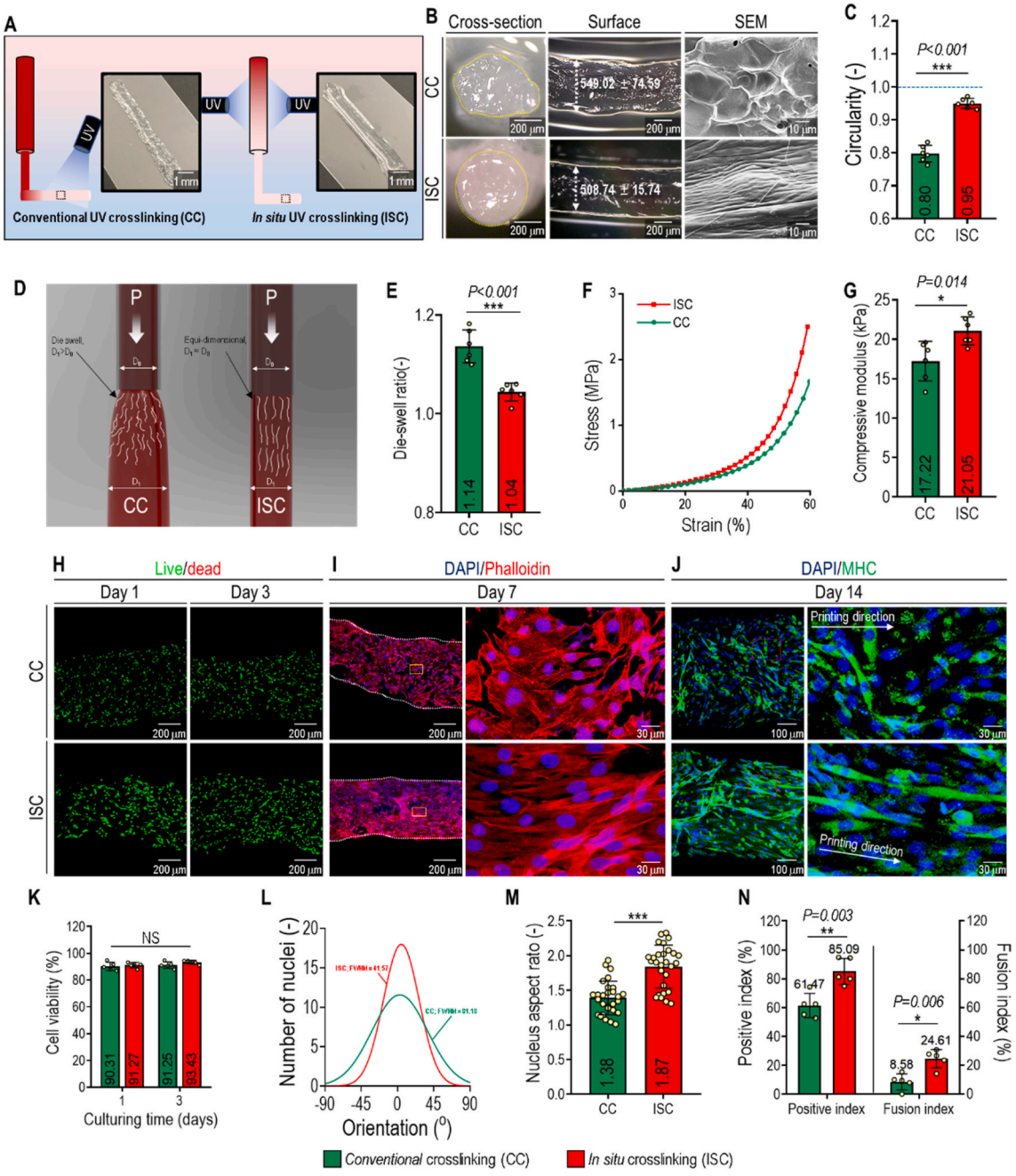

Fig. 6. (**A**) Fabrication schematic and (**B**) optical microscopy and SEM images of bio-constructs using in-situ crosslinking (ISC) and convention crosslinking (CC). (**C**) The circularity of ISC and CC structure. (**D**) Schematical illustration of extrudate swelling, (**E**) calculated extrudate-swell ratio (D_0/D_1, D_0 = nozzle diameter, and D_1 = strut diameter). (**F**) Compressive stress-strain curves and (**G**) calculated modulus of ISC and CC structure. (**H**) Live (green)/dead (red) at day 1 and 3, (**I**) DAPI (blue)/phalloidin (red) at day 7, and (**J**) DAPI (blue)/MHC (green) at day 14. (**K**) Cell viability at days 1 and 3. (**L**) Nucleus orientation distribution curve expressed in gaussian form and (**M**) aspect ratio at day 7. (**N**) MHC-positive and fusion index at day 14 (*$p < 0.05$, **$p < 0.005$, and ***$p < 0.001$). (For interpretation of the references to color in this figure legend, the reader is referred to the Web version of this article.)

was performed homogeneously.

In general, extrudate swelling can induce the randomization of the alignment of GelMa molecular chains, so that the minimization of extrudate swelling can be an important strategy to achieve a high degree of GelMa alignment (Fig. 6D). Fig. 6E shows a comparison of the extrudate swelling (D_1/D_o) structures fabricated using bioprinting with the CC and ISC processes. As expected, the extrudate-swell phenomenon caused the CC system to have a significantly higher die−swell ratio (1.14) compared to 1.04 for the ISC system, indicating that the aligned GelMa molecular chains prepared using the ISC process within the nozzle can be more stably sustained after extrusion than those prepared by the CC process. As such, structure crosslinked with the CC system is measured to be 1.08-fold larger with more variation compared to the ISC system (Fig. 6B).

Fig. 6F shows the stress-strain curves in a compressive mode. The compressive moduli of the structures constructed with CC and ISC were measured to be 17.22 and 21.05 kPa, respectively (Fig. 6G). In addition, the tensile modulus of CC and ISC constructs were measured to be 5.18 and 6.34 kPa, respectively (Supplementary Fig S2A and B). This phenomenon can be attributed to the more homogeneous crosslinking of the structure using the ISC process, which can lead to a more effective distribution of the external load than the CC structure.

To conduct biological evaluations of the two systems (CC and ISC), the printed structures were stained with live (green)/dead (red) at 1 and 3 days (Fig. 6H), DAPI (blue)/phalloidin (red) at 7 days (Fig. 6I), and DAPI (blue)/MHC (green) at 14 days (Fig. 6J). Cell viability was higher than 90%, indicating that both crosslinking systems were safe (Fig. 6K).

The orientation (Fig. 6L) and aspect ratio (Fig. 6M) of nuclei were analyzed using DAPI images after 7 days of culture. The orientation (FWHM) and aspect ratio on ISC were much higher in the ISC structure (51.57° and 1.87, respectively) than in the CC structure (81.18° and 1.38), respectively. This phenomenon can be attributed to the lower extrudate swelling ratio caused by the homogeneous crosslinking ISC process.

Several researchers have demonstrated that the anisotropic nuclear structure can be an indicator of the myogenic transcription factor due to the stresses caused by F-actin and microtubules [40,41]. Consequently, MHC expression on the ISC structure was 1.38-fold and 2.86-fold higher with respect to MHC positivity and fusion index (Fig. 6N). This phenomenon could be attributed to the significantly higher cellular alignment on ISC, which induces elevated levels of cell−cell interactions [11,14,42].

Previous works have demonstrated in myogenic differentiating capabilities of adipose stem cells (hASCs) under appropriate microcellular environmental conditions including stiffness and biochemical composition. To assess the myogenic differentiating capabilities of the ISC system, we carried out detailed analysis with hASCs-ladened GelMA construct using the optimized parameters (barrel temp = 4 °C, UV configuration = config-2, UV dosage = 821 mJ/cm^2, and wall shear stress = 625 Pa) (Fig. 7). The live (green)/dead (red) and DAPI (blue)/phalloidin (red) images, shown in Fig. 7, was used to quantitatively assess the cell viability and orientation factor of hASCs inside the GelMA construct. As expected, the cell viability (day 1 and 3) was relatively high (>90%) for both CC and ISC construct, indicating that both crosslinking systems were safe to hASCs (Fig. 7B). Moreover, as shown in Fig. 7C and D, the orientation factor and aspect ratio were significantly higher for ISC structure (0.70 and 1.97, respectively) compared to CC structure (0.37 and 1.38**),** indicating similar hASCs alignment compared to C2C12 myoblasts (Fig. 6).

To analyze the degree of myogenesis of the hASCs, the CC- and ISC-structures were stained with DAPI (blue)/MHC (green) immunofluorescence and quantitatively analyzed for MHC positive (Fig. 7F).

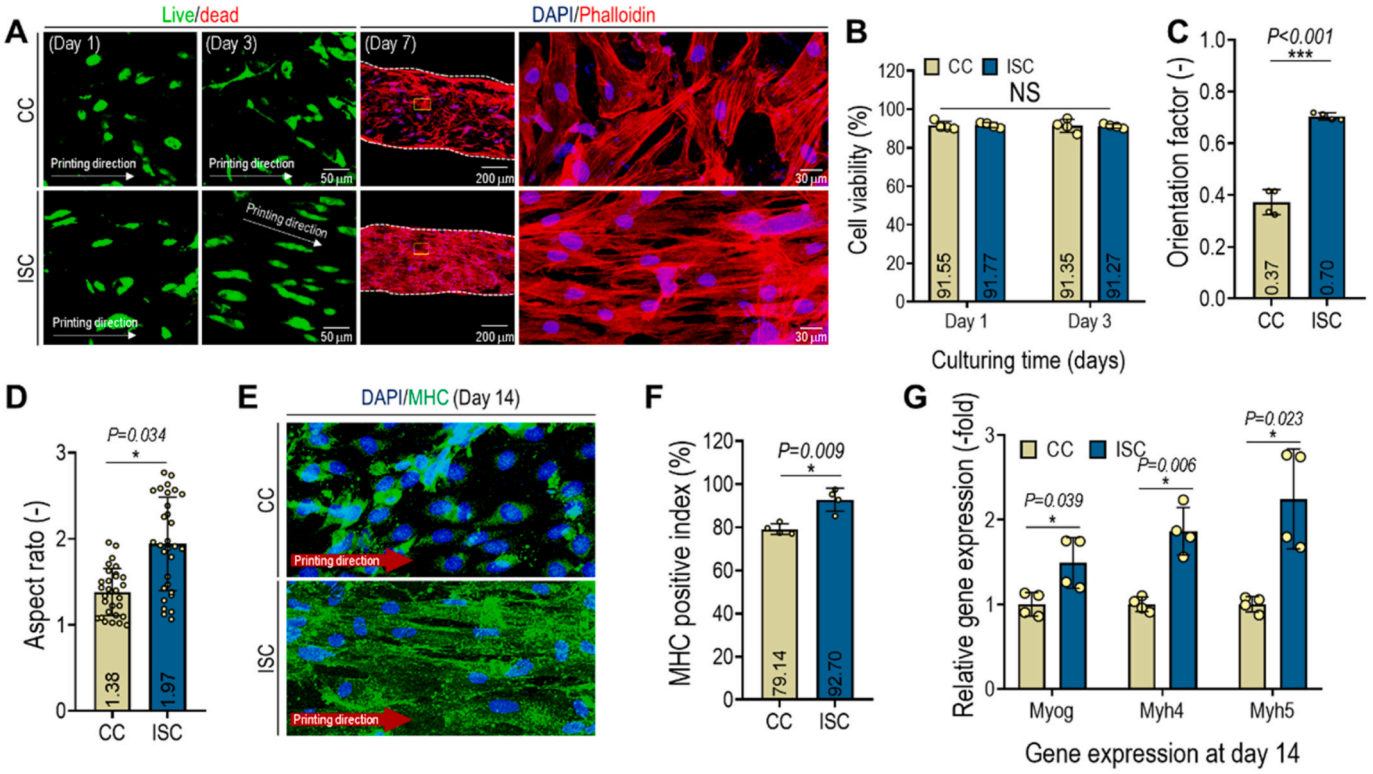

Fig. 7. (**A**) Live (green)/dead (red) at day 1 and 3 and DAPI (blue)/phalloidin (red) images at day 7 of CC and ISC muscle construct with human adipose stem cells (hASCs). Quantitative analysis of (**B**) cell viability (%), (**C**) orientation factor, and (**D**) aspect ratio of CC and ISC muscle construct. (**E**) Immunofluorescence images of DAPI (blue)/MHC (green) and (**F**) quantitative analysis of MHC positive index at 14 d of culture. (**G**) Relative gene expression of Myog, Myh4, and Myh5 of hASCs in CC- and ISC- structures at 14 d of culture (*$p < 0.05$, **$p < 0.005$, and ***$p < 0.001$). (For interpretation of the references to color in this figure legend, the reader is referred to the Web version of this article.)

Consequently, MHC positive index was 1.17-fold higher for the ISC structure compared to the CC structure. In addition, the myogenic gene (Myog, Myh4, and Myh5) expressions were significantly higher in ISC-structure (Fig. 7G). Based on the presented data, we predict that the optimized parameters affected similarly to hASCs compared to C2C12 myoblasts.

The present study has elaborated upon the work conducted by Ouyang et al. *via* investigating various print parameters such as barrel temperature, wall shear stress, UV doses, and UV configurations and achieve ideal cellular alignment. However, the current work could be expanded in regards to the assessments of C2C12 myoblasts or hASCs maturation. Previous studies have demonstrated that spontaneous contraction *via* electrical stimulation and the presence of striated sarcomeric patterns are good indicators of maturation [43,44].

3.6. *In vivo works*

The regenerative potential of the *in situ* crosslinking 3D bio-construct laden with human adipose stem cells (hASCs) was evaluated in a mouse model of VML injury. hASCs were selected for their high abundance, and various researchers have demonstrated the regenerative factors of skeletal muscle [4,45,46]. The VML defect was introduced by removing

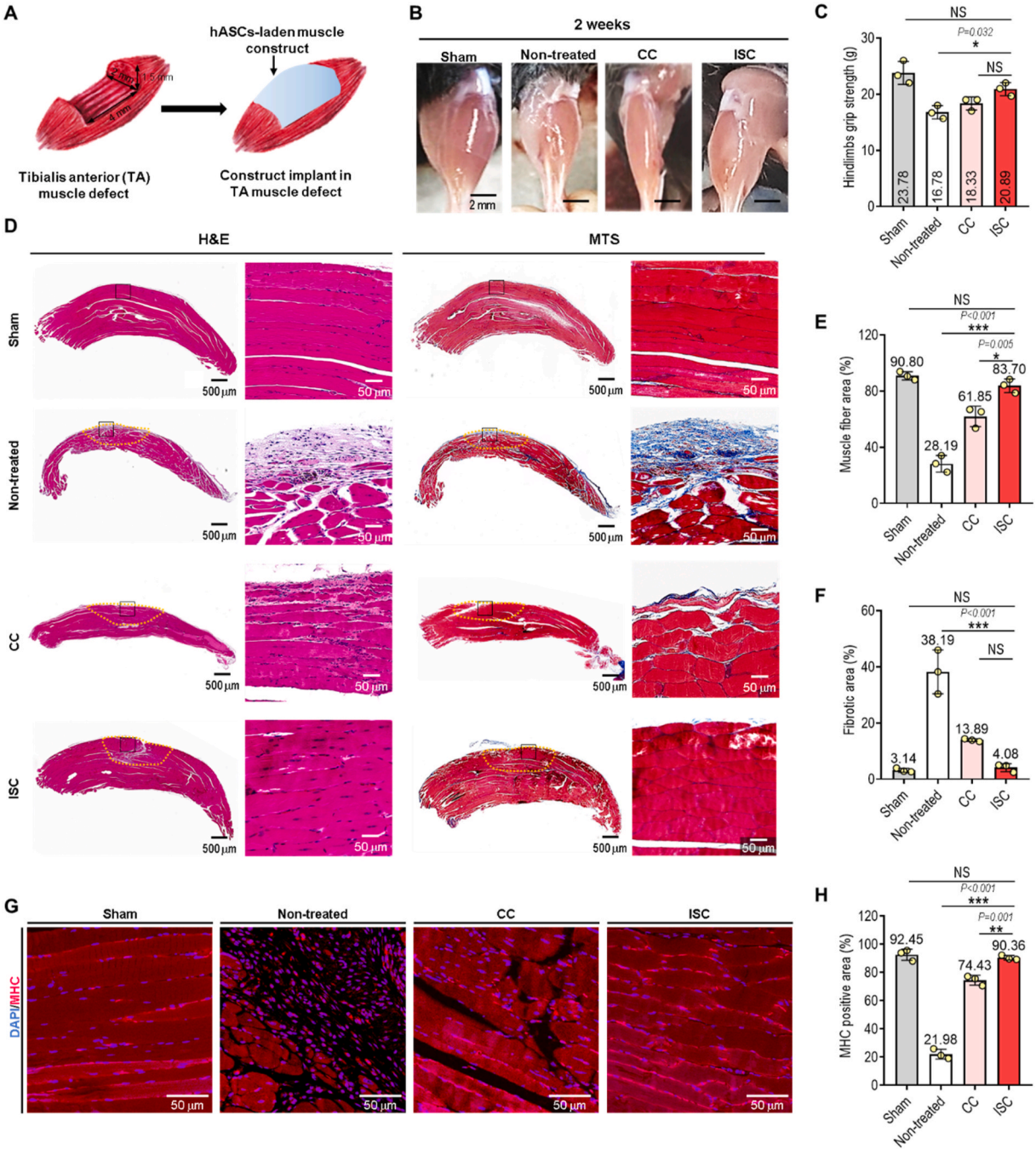

Fig. 8. (**A**) Schematic of implantation of hASC-laden muscle construct on VML defect on TA. (**B**) Optical images of TA and (**C**) hindlimb grip strength at 2 weeks post implantation. (**D**) H&E and MTS of transplanted sites (yellow dotted line indicates defect region). Calculated (**E**) muscle fiber area and (**F**) fibrotic area. (**G**) Immunochemical staining of DAPI (blue)/MHC (red) and (**H**) calculated percentage MHC coverage. (n = 3, NS = no significance, *p < 0.05, **p < 0.005, and ***p < 0.001). (For interpretation of the references to color in this figure legend, the reader is referred to the Web version of this article.)

the EDL/EHL, inducing 40% TA muscle loss. As shown in Figs. 8A and 3D bio-printed constructs sized 2 × 1.5 × 4 mm^3 were implanted onto the TA defect. To evaluate the muscle regenerative efficacy of the fabricated bio-construct using the ISC system, four groups were compared: (i) sham (no defect), (ii) non-treated (only defect), (iii) CC group (treated with conventionally crosslinked structure), and (iv) ISC group (treated with *in situ* crosslinked structure) (Fig. 8B).

Each group was evaluated *via* hindlimb grip testing (Fig. 8C) at two weeks post implantation. The grip strength of the group that received CC and ISC muscle construct was 1.09- fold and 1.24- fold higher compared to the non-treated group ($p = 0.037$). In addition, insignificant grip strength differences ($p = 0.126$) were measured compared to the ISC group and sham group, indicating that the implantation of ISC bio-construct had restored the physical capacity of TA defects.

To further analyze muscular regeneration, the implanted sites were histologically analyzed with H&E and Masson's trichrome staining (MTS) (Fig. 8D). Histological images were quantitatively evaluated for muscle fiber and fibrotic areas (Fig. 8E and F, respectively). As expected,

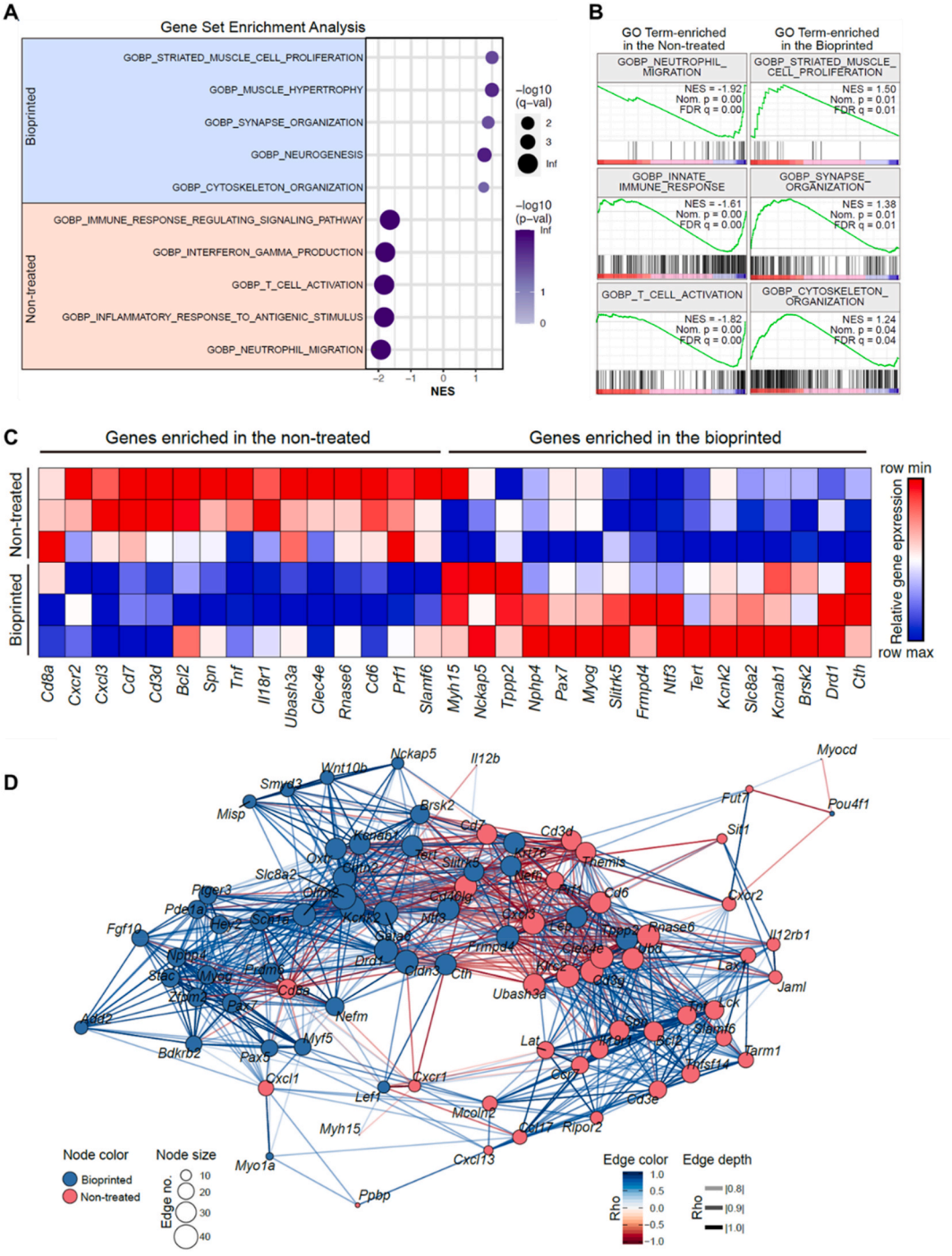

Fig. 9. (**A**) Bubble plot and (**B**) enrichment plots show the results of GSEA. In the bubble plot, the X-axis, the size of, and the color of bubbles indicate normalized enrichment score (NES), false discovery rate q-value, and nominal p-value, respectively. Enrichment plots were generated by GSEA software. (**C**) Heatmap showing the relative expression representative genes of the top enriched GO terms. (**D**) Gene neatwork showing correlations (Spearman's Rho > |0.8|) among genes enriched in the non-treated and bioprinted groups. The color and size of each node show the group and the number of edges having. The color and depth of each edge show Spearman's Rho. (For interpretation of the references to color in this figure legend, the reader is referred to the Web version of this article.)

significantly higher muscle regeneration was observed in both the bio-printed groups (CC and ISC) compared to the defect group. In particular, the group that received the ISC muscle construct exhibited 3-fold and 1.4-fold higher muscle fiber area compared to the defect and CC group, respectively, indicating that the aligned muscle construct has significantly accelerated muscle regeneration. Moreover, the percentage muscle fiber area was not significantly different from that in the sham group, indicating restoration of the VML defects.

In general, extensive damage to skeletal muscles, such as VML defects in the TA can cause excess deposition of collagen, leading to fibrosis. To quantify the degree of fibrosis, the blue area in MT staining was analyzed. As a result, the bio-printed groups (CC and ISC) showed a significant reduction in fibrosis compared to the non-treated group.

To confirm that the aligned muscle construct could accelerate muscle regeneration, the muscle sections were stained with antibodies to MHC (Fig. 8G). The immunostaining revealed that MHC protein was highly expressed in mice implanted for both the bio-constructs (CC and ISC) compared to defect (Fig. 8H). However, MHC positive area for the anisotropic muscle construct (ISC) was significantly higher (1.2-fold, $p = 0.001$) compared to the isotropic muscle construct (CC). Based on the physical and histological results, we confirmed the efficacy of the muscle constructs fabricated using the ISC method for accelerated muscle regeneration.

3.7. RNA sequencing

To validate the phenotypic and histologic analyses, RNA-seq analysis was performed using total RNAs isolated from TA muscles of the non-treated and the bioprinted groups. To avoid any batch effect, total RNAs were prepared from the entire TA muscles, and the RNA library was prepared as described in the method section. Using six-transcriptomes (3 per each group), we performed the genome-wide unbiased Gene Set Enrichment Analysis (GSEA, Broad Institute) [47]. In line with the phenotypic and histologic analyses (Fig. 9), GSEA shows that Gene Ontology (GO) terms related to muscle function, regeneration, and hypertrophy (i.e., STRIATED MUSCLE CELL PROLIFERATION, MUSCLE HYPERTROPHY, SYNAPSE ORGANIZATION, NEUROGENESIS, and CYTOSKELETON ORGANIZATION) were enriched in the bioprinted group, whereas inflammation-related GO terms (IMMUNE RESPONSE REGULATING SIGNALING PATHWAY, INTERFERON GAMMA PRODUCTION, T CELL ACTIVATION, INFLAMMATORY RESPONSE TO ANTIGENIC STIMULUS, and NEUTROPHIL MIGRATION) were enriched in the non-treated group (Fig. 9A–D), supporting the phenotypic and histologic analyses. The network analysis based on Spearman's correlation (Rho $> |0.8|$) presented that those genes enriched in the bioprinted group have negative correlations with genes enriched in the non-treated group (Fig. 9D). Together, our biological analyses confirmed the efficacy of muscle regeneration.

4. Conclusion

Herein, we successfully developed a GelMa structure laden with uniaxially aligned C2C12 cells *via* an *in situ* crosslinking process during the extrusion for use in volumetric muscle regeneration. The UV exposure dose, wall shear stress, and the number of UV sources were investigated to obtain appropriate biophysical and cellular activities, such as cell growth, cell alignment, and myogenic activities. The optimized printing parameters [barrel temperature = 4 °C, dual UV light source (config-2), UV dose = 821 mJ/cm^2, wall shear stress = 625 Pa] of *in situ* crosslinking system (ISC) system allows a significant reduction in the extrudate swelling phenomenon, resulting in a higher degree of cellular alignment and MHC expression compared to the conventionally cross-linked (CC) structure. Additionally, after optimizing the printing parameters with C2C12, we have performed additional experimenters to ensure similar effects with hASCs. Then, *in vivo* implantation of the ISC structure ladened with hASCs into a mouse model of VML showed that muscle regeneration was significantly improved compared to CC structure. Based on the efficacy of our results, we conclude that the newly designed *in situ* crosslinked GelMa construct shows considerable promise as an effective treatment option for VML.

CRediT authorship contribution statement

Hanjun Hwangbo: Conceptualization, Methodology, Investigation, Writing – original draft. **Hyeongjin Lee:** Conceptualization, Methodology, Investigation, Writing – original draft. **Eun-Ju Jin:** Methodology, Investigation, Writing – original draft. **JaeYoon Lee:** Methodology, Investigation. **Yunju Jo:** Investigation. **Dongryeol Ryu:** Methodology, Writing – review & editing, Supervision. **GeunHyung Kim:** Conceptualization, Methodology, Writing – review & editing, Supervision.

Declaration of competing interest

The authors (Hanjun Hwangbo, Hyeongjin Lee, Eun-Ju Jin, JaeYoon Lee, Yunju Jo, Dongryeol Ryu, GeunHyung Kim) declare that they have no known competing financial interests or personal relationships that could have appeared to influence the work reported in this paper.

Acknowledgments

This study was supported by a grant from the National Research Foundation of Korea funded by the Ministry of education, Science, and Technology (MEST) (Grant NRF-2018R1A2B2005263) and supported by the National Research Foundation of Korea (NRF) Grant funded by the Ministry of Science and ICT for Bioinspired Innovation Technology Development Project (NRF-2018M3C1B7021997). This study was also supported by a grant from the Ministry of Trade, Industry & Energy (MOTIE, Korea) under Industrial Technology Innovation Program (20009652: Technology on commercialization and materials of Bio-absorbable Hydroxyapatite that is less than micrometer in size).

Appendix A. Supplementary data

Supplementary data to this article can be found online at https://doi.org/10.1016/j.bioactmat.2021.06.031.

References

[1] B.F. Grogan, J.R. Hsu, S.T.R. Consortium, Volumetric muscle loss, J AM ACAD ORTHOP SUR 19 (2011) S35–S37.
[2] C.L. Ward, L. Ji, B.T. Corona, An autologous muscle tissue expansion approach for the treatment of volumetric muscle loss, BioResearch open access 4 (1) (2015) 198–208.
[3] K.H. Nakayama, M. Quarta, P. Paine, C. Alcazar, I. Karakikes, V. Garcia, O. J. Abilez, N.S. Calvo, C.S. Simmons, T.A. Rando, Treatment of volumetric muscle loss in mice using nanofibrillar scaffolds enhances vascular organization and integration, Commun. Biol. 2 (1) (2019) 1–16.
[4] S.-V. Forcales, Potential of adipose-derived stem cells in muscular regenerative therapies, Front. Aging Neurosci. 7 (2015) 123.
[5] M. Quarta, M. Cromie, R. Chacon, J. Blonigan, V. Garcia, I. Akimenko, M. Hamer, P. Paine, M. Stok, J.B. Shrager, Bioengineered constructs combined with exercise enhance stem cell-mediated treatment of volumetric muscle loss, Nat. Commun. 8 (1) (2017) 1–17.
[6] Y.-J. Choi, Y.-J. Jun, D.Y. Kim, H.-G. Yi, S.-H. Chae, J. Kang, J. Lee, G. Gao, J.-S. Kong, J. Jang, A 3D cell printed muscle construct with tissue-derived bioink for the treatment of volumetric muscle loss, Biomaterials 206 (2019) 160–169.
[7] A. Shapira, N. Noor, M. Asulin, T. Dvir, Stabilization strategies in extrusion-based 3D bioprinting for tissue engineering, Appl. Phys. Rev. 5 (4) (2018), 041112.
[8] S. Rhee, J.L. Puetzer, B.N. Mason, C.A. Reinhart-King, L.J. Bonassar, 3D bioprinting of spatially heterogeneous collagen constructs for cartilage tissue engineering, ACS Biomater. Sci. Eng. 2 (10) (2016) 1800–1805.
[9] P.D. Tatman, W. Gerull, S. Sweeney-Easter, J.I. Davis, A.O. Gee, D.-H. Kim, Multiscale biofabrication of articular cartilage: bioinspired and biomimetic approaches, Tissue Eng. B Rev. 21 (6) (2015) 543–559.
[10] L. Ouyang, C.B. Highley, W. Sun, J.A. Burdick, A generalizable strategy for the 3D bioprinting of hydrogels from nonviscous photo-crosslinkable inks, Adv. Mater. 29 (8) (2017), 1604983.
[11] W. Kim, G. Kim, 3D bioprinting of functional cell-laden bioinks and its application for cell-alignment and maturation, Appl. Mater. Today 19 (2020), 100588.

[12] W. Kim, G. Kim, A functional bioink and its application in myoblast alignment and differentiation, Chem. Eng. J. 366 (2019) 150–162.
[13] W. Kim, C.H. Jang, G.H. Kim, A myoblast-laden collagen bioink with fully aligned Au nanowires for muscle-tissue regeneration, Nano Lett. 19 (12) (2019) 8612–8620.
[14] W. Kim, H. Lee, J. Lee, A. Atala, J.J. Yoo, S.J. Lee, G.H. Kim, Efficient myotube formation in 3D bioprinted tissue construct by biochemical and topographical cues, Biomaterials 230 (2020), 119632.
[15] H. Lee, W. Kim, J. Lee, K.S. Park, J.J. Yoo, A. Atala, G.H. Kim, S.J. Lee, Self-aligned myofibers in 3D bioprinted extracellular matrix-based construct accelerate skeletal muscle function restoration, Appl. Phys. Rev. 8 (2) (2021), 021405.
[16] X. Wu, B.T. Corona, X. Chen, T.J. Walters, A standardized rat model of volumetric muscle loss injury for the development of tissue engineering therapies, BioResearch open access 1 (6) (2012) 280–290.
[17] D. Ryu, H. Zhang, E.R. Ropelle, V. Sorrentino, D.A. Mázala, L. Mouchiroud, P. L. Marshall, M.D. Campbell, A.S. Ali, G.M. Knowels, NAD+ repletion improves muscle function in muscular dystrophy and counters global PARylation, Sci. Transl. Med. 8 (361) (2016), 361ra139-361ra139.
[18] B. Li, C.N. Dewey, RSEM: accurate transcript quantification from RNA-Seq data with or without a reference genome, BMC Bioinf. 12 (1) (2011) 1–16.
[19] H. Kim, S.C. Cho, H.J. Jeong, H.Y. Lee, M.H. Jeong, J.H. Pyun, D. Ryu, M. Kim, Y. S. Lee, M.S. Kim, Indoprofen prevents muscle wasting in aged mice through activation of PDK1/AKT pathway, J. Cachexia Sarcopenia Muscle 11 (4) (2020) 1070–1088.
[20] A.I. Van Den Bulcke, B. Bogdanov, N. De Rooze, E.H. Schacht, M. Cornelissen, H. Berghmans, Structural and rheological properties of methacrylamide modified gelatin hydrogels, Biomacromolecules 1 (1) (2000) 31–38.
[21] A.M. Collinsworth, S. Zhang, W.E. Kraus, G.A. Truskey, Apparent elastic modulus and hysteresis of skeletal muscle cells throughout differentiation, Am. J. Physiol. Cell Physiol. 283 (4) (2002) C1219–C1227.
[22] A.J. Engler, M.A. Griffin, S. Sen, C.G. Bonnemann, H.L. Sweeney, D.E. Discher, Myotubes differentiate optimally on substrates with tissue-like stiffness pathological implications for soft or stiff microenvironments, J. Cell Biol. 166 (6) (2004) 877–887.
[23] J. Cadet, E. Sage, T. Douki, Ultraviolet radiation-mediated damage to cellular DNA, Mutat. Res. 571 (1–2) (2005) 3–17.
[24] R. Brem, M. Guven, P. Karran, Oxidatively-generated damage to DNA and proteins mediated by photosensitized UVA, Free Radic. Biol. Med. 107 (2017) 101–109.
[25] C. Lee, C.D. O'Connell, C. Onofrillo, P.F. Choong, C. Di Bella, S. Duchi, Human articular cartilage repair: sources and detection of cytotoxicity and genotoxicity in photo-crosslinkable hydrogel bioscaffolds, Stem Cells Transl Med 9 (3) (2020) 302–315.
[26] H.-L. Lo, S. Nakajima, L. Ma, B. Walter, A. Yasui, D.W. Ethell, L.B. Owen, Differential biologic effects of CPD and 6-4PP UV-induced DNA damage on the induction of apoptosis and cell-cycle arrest, BMC Canc. 5 (1) (2005) 1–9.
[27] J. Cadet, T. Douki, Formation of UV-induced DNA damage contributing to skin cancer development, Photochem. Photobiol. Sci. 17 (12) (2018) 1816–1841.
[28] H. Sterenborg, J. Van der Leun, Tumorigenesis by a long wavelength UV-A source, Photochem, Photobiol 51 (3) (1990) 325–330.
[29] N.F. Huang, S. Patel, R.G. Thakar, J. Wu, B.S. Hsiao, B. Chu, R.J. Lee, S. Li, Myotube assembly on nanofibrous and micropatterned polymers, Nano Lett. 6 (3) (2006) 537–542.
[30] H. Hwangbo, W. Kim, G.H. Kim, Lotus-root-Like microchanneled collagen scaffold, ACS Appl. Mater. Interfaces 13 (11) (2020) 12656–12667.
[31] E. Michalaki, V.N. Surya, G.G. Fuller, A.R. Dunn, Perpendicular alignment of lymphatic endothelial cells in response to spatial gradients in wall shear stress, Comm. Biol. 3 (1) (2020) 1–9.
[32] H. Aubin, J.W. Nichol, C.B. Hutson, H. Bae, A.L. Sieminski, D.M. Cropek, P. Akhyari, A. Khademhosseini, Directed 3D cell alignment and elongation in microengineered hydrogels, Biomaterials 31 (27) (2010) 6941–6951.
[33] T. Distler, A.A. Solisito, D. Schneidereit, O. Friedrich, R. Detsch, A.R. Boccaccini, 3D printed oxidized alginate-gelatin bioink provides guidance for C2C12 muscle precursor cell orientation and differentiation via shear stress during bioprinting, Biofabrication 12 (4) (2020), 045005.
[34] M. Hospodiuk, M. Dey, D. Sosnoski, I.T. Ozbolat, The bioink: a comprehensive review on bioprintable materials, Biotechnol. Adv. 35 (2) (2017) 217–239.
[35] C.S. Chen, M. Mrksich, S. Huang, G.M. Whitesides, D.E. Ingber, Geometric control of cell life and death, Science 276 (5317) (1997) 1425–1428.
[36] R. McBeath, D.M. Pirone, C.M. Nelson, K. Bhadriraju, C.S. Chen, Cell shape, cytoskeletal tension, and RhoA regulate stem cell lineage commitment, Dev. Cell 6 (4) (2004) 483–495.
[37] B. Murtuza, J.W. Nichol, A. Khademhosseini, Micro-and nanoscale control of the cardiac stem cell niche for tissue fabrication, Tissue Eng. B Rev. 15 (4) (2009) 443–454.
[38] C.M. Nelson, C.S. Chen, Cell-cell signaling by direct contact increases cell proliferation via a PI3K-dependent signal, FEBS Lett. 514 (2–3) (2002) 238–242.
[39] R. Chang, J. Nam, W. Sun, Effects of dispensing pressure and nozzle diameter on cell survival from solid freeform fabrication–based direct cell writing, Tissue Eng. 14 (1) (2008) 41–48.
[40] S. Ahadian, J. Ramón-Azcón, S. Ostrovidov, G. Camci-Unal, V. Hosseini, H. Kaji, K. Ino, H. Shiku, A. Khademhosseini, T. Matsue, Interdigitated array of Pt electrodes for electrical stimulation and engineering of aligned muscle tissue, Lab Chip 12 (18) (2012) 3491–3503.
[41] K. Haase, J.K. Macadangdang, C.H. Edrington, C.M. Cuerrier, S. Hadjiantoniou, J. L. Harden, I.S. Skerjanc, A.E. Pelling, Extracellular forces cause the nucleus to deform in a highly controlled anisotropic manner, Sci. Rep. 6 (1) (2016) 1–11.
[42] W. Kim, M. Kim, G.H. Kim, 3D-printed biomimetic scaffold simulating microfibril muscle structure, Adv. Funct. Mater. 28 (26) (2018), 1800405.
[43] Y. Manabe, S. Miyatake, M. Takagi, M. Nakamura, A. Okeda, T. Nakano, M. F. Hirshman, L.J. Goodyear, N.L. Fujii, Characterization of an acute muscle contraction model using cultured C2C12 myotubes, PloS One 7 (12) (2012), e52592.
[44] H. Kaji, T. Ishibashi, K. Nagamine, M. Kanzaki, M. Nishizawa, Electrically induced contraction of C2C12 myotubes cultured on a porous membrane-based substrate with muscle tissue-like stiffness, Biomaterials 31 (27) (2010) 6981–6986.
[45] A. Gorecka, S. Salemi, D. Haralampieva, F. Moalli, D. Stroka, D. Candinas, D. Eberli, L. Brügger, Autologous transplantation of adipose-derived stem cells improves functional recovery of skeletal muscle without direct participation in new myofiber formation, Stem Cell Res. Ther. 9 (1) (2018) 1–12.
[46] I. Grabowska, M. Zimowska, K. Maciejewska, Z. Jablonska, A. Bazga, M. Ozieblo, W. Streminska, J. Bem, E. Brzoska, M.A. Ciemerych, Adipose tissue-derived stromal cells in matrigel impact the regeneration of severely damaged skeletal muscles, Int. J. Mol. Sci. 20 (13) (2019) 3313.
[47] A. Subramanian, P. Tamayo, V.K. Mootha, S. Mukherjee, B.L. Ebert, M.A. Gillette, A. Paulovich, S.L. Pomeroy, T.R. Golub, E.S. Lander, Gene set enrichment analysis: a knowledge-based approach for interpreting genome-wide expression profiles, Proc. Natl. Acad. Sci. Unit. States Am. 102 (43) (2005) 15545–15550.